IEEE Sensors Council IEEE SENSORS JOURNAL, VOL. 25, NO. 13, 1 JULY 2025

Flexible Multilevel Hierarchical Architectural Integrated Pressure-Temperature Sensor With High Sensitivity, Wide Working Range, and Independent Stimulus Discriminability

Shuning Chen, Xu Wang, Bozhi Wu, Jiahong Kang, Ji Zhou, Meng Nie, and Litao Sun, *Member, IEEE*

***Abstract*—Wearable multifunctional sensors have attracted favorable attention due to their promising applications in artificial limbs, health monitoring, and human–machine interfaces. However, developing the intrinsic integrating sensors embowed multiparameters independently decoupled is still a critical challenge. Here, a multilevel hierarchical architectural integrated dual-functional sensor with shared electrodes is proposed to decouple pressure and temperature signals independently. The capacitive pressure-sensitive layer is constructed by the designed unique dot-knot micro-structures to obtain the multilevel hierarchical architecture with the thermoplastic polyurethane@polyaniline (TPU@PANI) membrane. The designed micro-structures effectively realize the pressure sensing in stage to obtain an ultra-wide measurement range and an ultralow pressure detection. Meanwhile, the hierarchical micro-structure buffers the pressure acting on the temperature-sensitive layer to solve the signal crosstalk. The resistive temperature-sensitive layer is formed with a serpentine-shaped nickel oxide (NiO) film based on the negative temperature coefficient (NTC) effect by microelectronic printing. The proposed sensor processes an ultra-wide pressure range of 23 MPa, high linearity values of 0.998 and 0.991 in ranges of 0–580 kPa and 10–23 MPa, an ultralow pressure detection limit of 3 Pa, and a high temperature sensitivity of −1.85%/°C over 25 °C–60 °C. Demonstrations of the presented flexible integrated sensor to monitor vocalization, motion, breathing, and object grabbing/releasing in various application scenarios involving coupled pressure/temperature stimuli exhibited its excellent potential capabilities in wearable electronics.**

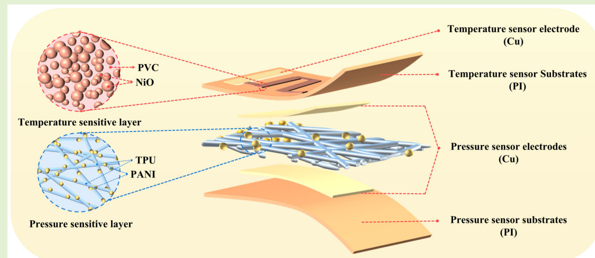

***Index Terms*— Dual-functional sensor, high sensitivity, independent decoupling, integrated sensor, wide range.**

I. Introduction

As THE largest information interaction medium between the human body and the environment, the skin acquires and responds to external stimuli through various types of receptors (e.g., pressure, temperature, strain, etc.), enabling the assessment of health and motion. Pressure sensing can monitor blood pressure, heart rate, pulse, and respiration, which is widely used in daily healthcare [1], [2]. Temperature sensing can detect fever and infections, aiding in the prevention and identification of abnormal respiratory symptoms caused by conditions such as respiratory diseases or poisoning [3], [4]. Traditional MEMS pressure sensors, based on silicon micromachining technology, have achieved mature performance in sensitivity, temperature stability, and long-term reliability through structural optimization, material innovation, and process improvement. Xu et al. [5] proposed a MEMS pressure sensor with a convex diaphragm combined with a peninsula-island structure, achieving a high sensitivity of 0.065 mV/V/Pa in the ultralow pressure range (0–500 Pa), a nonlinearity error as low as 0.30% FS, and an exceptional overload capacity of 21 000%FS. Xu et al. [6] further enhanced the sensitivity to 2.255 mV/V/kPa using a silicon-on-insulator (SOI) structure, while ensuring high-temperature stability (20 °C–160 °C, TCS of −0.221%FS/°C) through an ultra-thin single-crystal silicon layer (1.5 μm) and CMOS-compatible processes. Additionally, Mikhail Basov [7], [8] focused on the long-term

Received 20 April 2025; revised 12 May 2025; accepted 13 May 2025. Date of publication 22 May 2025; date of current version 2 July 2025. This work was supported in part by the National Natural Science Foundation of China under Grant 62274031 and Grant T2321002 and in part by Jiangsu Provincial Natural Science Foundation of China under Grant BK20243023. The associate editor coordinating the review of this article and approving it for publication was Prof. Wei-Chen Huang. *(Corresponding author: Meng Nie.)*

This work involved human subjects in its research. Approval of all ethical and experimental procedures and protocols was granted by the Southeast University.

The authors are with the SEU-FEI Nano-Pico Center, Key Laboratory of MEMS of Ministry of Education, Southeast University, Nanjing, Jiangsu 210096, China (e-mail: m_nie@seu.edu.cn).

This article has supplementary downloadable material available at https://doi.org/10.1109/JSEN.2025.3570787, provided by the authors.

Digital Object Identifier 10.1109/JSEN.2025.3570787

stability of traditional pressure sensors, demonstrating that the performance degradation (e.g., sensitivity, nonlinearity, and temperature hysteresis) of MEMS pressure sensors after three to five years does not exceed 1.5%. The study highlights the unidirectional influence of residual mechanical stresses root mean squares (rms) from the pressure sensor assembly design on sensitivity and nonlinearity under varying pressure directions and temperature hysteresis errors. By optimizing diaphragm geometries (e.g., beams, grooves, protrusions) and incorporating functional materials, MEMS pressure sensors exhibit excellent stress concentration and linearity control [9]. Traditional MEMS temperature sensors offer high precision (±0.1 °C), miniaturization (<1 mm^2), low power consumption (μW level), making them suitable for medical and industrial precision temperature measurement. Yuan et al. [10] proposed a novel MEMS temperature sensor based on a piezoelectric film resonator, achieving a sensitivity of −660 ppm/°C and a temperature resolution of 10 μK. Ji et al. [11] demonstrated a high-precision active wireless MEMS temperature sensor with a dynamic range from −40 °C to 180 °C and a minimum sensitivity better than 0.011 °C across this wide temperature range. With the increasing complexity of intelligent sensing demands, single-function sensors are no longer sufficient for multiscenario applications, making dual-function sensors integrating temperature and pressure detection a research hotspot. However, the rigidity of silicon-based materials limits their adaptability to flexible scenarios. Flexible sensors, with their lightweight design (weight <1 g/cm^2) and excellent conformability, are suitable for dynamic applications such as wearable devices and biomedical monitoring. They also simplify packaging processes, reduce costs, and enable multimodal sensing through elastic materials, demonstrating irreplaceable potential in flexible electronics and robotic tactile systems. Flexible sensors integrating temperature and pressure sensing capabilities can comprehensively monitor physical changes in the human body, showing great promise in applications such as intelligent robotics [12], smart prosthetics [13], augmented/virtual reality (AR/VR) [14], disease diagnosis [15], and human–machine intelligent interaction [16].

Flexible multifunctional sensors need to be able to monitor and decouple multiple physical signals simultaneously. Currently, researchers have proposed three methods to solve the independent decoupling issue: distributed arrangement of devices, material selectivity for independent parameters, and integrated device structures [12], [17], [18]. Wang et al. [19] proposed a flexible temperature-pressure sensor based on a thermoelectric film and a porous microcone conductive elastomer, achieving a temperature sensitivity of 3.77 mV K^{-1}, a low-pressure detection limit of 16 Pa, and a pressure detection range of 0–11 kPa (sensitivity of 37 kPa^{-1}). By incorporating a flexible hydrogel heat sink into the thermoelectric device, temperature control was achieved, effectively decoupling temperature and pressure signals. Li et al. [20] reported a flexible pressure-temperature sensor based on a conductive microstructured metal-organic framework (MOF), with a pressure sensing range of up to 300 kPa (sensitivity of 61.61 kPa^{-1}, ultralow detection limit of 1 Pa) and a temperature sensitivity of 57.1 μV K^{-1}. Utilizing two distinct sensing principles, this sensor can distinguish and independently detect pressure and temperature stimuli. Bae et al. [21] designed a capacitive pressure sensing mechanism by introducing surface wrinkled microstructures and a temperature-insensitive material, Al2O3, which exhibited a linear high-pressure sensitivity of 0.7 kPa^{-1} up to 25 kPa and a resistance temperature coefficient of 0.83% K^{-1} within the temperature range of 22 °C–70 °C. Through innovative device design and the use of temperature-independent materials, the ability to differentiate between the two stimuli was successfully achieved. Zhu et al. [22] developed a flexible sandwich-structured dual-function sensor based on the organic piezoelectric material polyvinylidene fluoride (PVDF) and a thermoelectric polyaniline-based composite film, demonstrating a high temperature sensitivity of 45.5 μV K^{-1} and a pressure detection range of 0.125–10 kPa (sensitivity of 392 mV kPa^{-1}). With meticulous device design, this sensor can simultaneously or individually sense temperature and tactile stimuli. Although most reported multifunctional devices can recognize multiple parameters, including temperature and pressure, their designs still face significant limitations. For instance, some decoupled temperature-pressure sensors isolate thermal crosstalk by adding thermal barriers [23], rely on stringent material preparation processes, or simply stack two functional devices [19]. While these methods partially address signal crosstalk issues, they increase the structural complexity of the devices [24], [25], [26], hinder intrinsic functional integration, and may compromise sensor sensitivity [15], [27]. Therefore, achieving excellent sensing performance in integrated multifunctional flexible sensors while ensuring crosstalk-free signal responses remains a critical challenge in current research.

Herein, a dual-functional sensor based on integrating a fiber membrane based on the capacitive pressure principle and a film based on the negative temperature coefficient (NTC) resistive principle is proposed. Thermoplastic polyurethane@polyaniline (TPU@PANI) composite fiber membrane was fabricated by an electrostatic spinning process, and unique "dot" and "knot" micro-structures were designed by adjusting the doping ratio of PANI. The distinctive material modulation enabled the pressure-sensitive layer to extend the maximum range to 23 MPa with sensitivity enhanced 11 times higher than pure TPU fiber membrane. Meanwhile, the pressure sensor demonstrated an impressive linear response of 0.998 and 0.991 in ranges of 0–580 kPa and 10–23 MPa, as well as an ultralow pressure detection limit of 3 Pa. The temperature-sensitive layer employs microelectronic printing to form a serpentine-shaped nickel oxide (NiO) film on a polyimide (PI) substrate with the shared electrode. The dual-functional sensors possess a high sensitivity of −1.85%/°C, a fast response time of 1 s, and low hysteresis for temperature sensing. The temperature and pressure layers are rationally designed to be a sandwich-integrated structure by the shared electrodes. The dot-knot micro-structures in the pressure-sensitive fiber membrane effectively buffer the pressure acting on the temperature-sensitive layer, which solves the signal crosstalk between the temperature and pressure sensing. The presented design strategy for the integrated sensor and the way to achieve the independently decoupled parameters lay the groundwork for its application in artificial limbs, intelligent robots, human–machine interfaces, and health monitoring devices.

II. Results and Discussion

A. Structure Design and Working Mechanism

The design and material component selection are critical to realizing the independently decouplable performance of the pressure-temperature dual-functional sensor which leverages a multilevel hierarchical architecture [Fig. 1(a)]. NiO is a thermally sensitive material with a NTC, requiring neither an excessively thick functional layer nor a special structure like a thermocouple. The temperature-sensitive layer was fabricated by mixing NiO with polyvinyl chloride (PVC) to significantly increase the softness due to the low coefficient of thermal expansion of PVC (5×10^{-5} K^{-1}), while reducing the inter-material mismatch caused by the thermal expansion effect under the composite system. First, the printing precursor solution was obtained by mixing NiO and PVC with N, N-dimethylformamide dimethylformamide (DMF) as solvent under heating and stirring. A microelectronic printing process was used to print serpentine NiO films on PI substrates with shared electrodes. On the other hand, TPU fibers benefit from a porous fibrous structure and excellent elasticity, which allows for more compression variation when applied to the dielectric layer of capacitive pressure sensors. An innovative PANI@TPU fiber membrane was developed as a pressure-sensitive layer by mixing PANI and TPU into DMF and acetone with electrostatic spinning technology. The pressure-sensitive layer consists of hierarchical interlaced TPU fibers (with diameters of several hundred nanometers), and the pores inside the membrane provide the basis for excellent compressibility. PANI doping in the TPU allows the characteristic microstructures of "dots" and "knots" to be formed inside the hybrid fiber membrane. The dual-function sensor employs a customized flexible printed circuit (FPC) printed circuit board (PCB) substrate equipped with a shared electrode. The upper electrode of the pressure sensor is connected to the electrode of the temperature sensor through customized vias (flex vias). This design allows the encapsulation of the sensor to be completed simply by bonding two layers of PI substrates together. Additionally, it significantly simplifies the device testing process while enhancing the integration and reliability of the device. The pressure-temperature sensor adopts a sandwich structure: the NiO temperature-sensitive layer serves as the top layer, the shared electrode based on the PI substrate acts as the middle layer, and the PANI@TPU pressure-sensitive layer forms the bottom layer.

Fig. 1(b)–(d) demonstrates the dual-functional sensor exhibits good flexibility and sufficiently thin thickness, enabling it to adhere directly to the skin and accurately follow its deformation for real-time monitoring. The stacked integrated structure, with a compact device size of 15×15 mm and a thickness of 0.7 mm, is significantly smaller than the planar integrated structure. This design allows for precise simultaneous sensing of temperature and pressure signals at the same location, as illustrated in Fig. 1(e).

Individual particles of NiO are in contact with each other or maintain a characteristic distance of several hundred nanometers. The conductivity of NiO relies on a thermally activated process, wherein charge carriers must overcome a certain energy barrier to participate in conduction. As the temperature increases, more charge carriers are excited into the conduction band, leading to a significant decrease in resistance. This exponential growth in charge carrier concentration results in an exponential relationship between resistance and temperature. As a semiconductor material, the resistivity formula [28] for NiO is

$$\rho = \rho_0 \exp\left(-\frac{E_a}{B * T}\right) \tag{1}$$

where ρ is the conductivity at temperature T, E_a is the activation energy of the conductive material, B is the Boltzmann's constant, ρ_0 is the pre-exponential factor (related to the intrinsic properties of the material), and the T is the absolute temperature (in Kelvin). NiO acts as a p-type semiconductor [29] with a forbidden bandwidth of 3.7 eV. The electron transition produces more valence band holes when the temperature increases, and the increased number of carriers leads to the decreased resistivity of the material. Meanwhile, due to the proximity (several hundred nanometers) between the NiO nanoparticles, the electrons tunnel between the neighboring NiO nanoparticles during transport [Fig. 1(f)]. The probability of electron tunneling D can be defined [30] as

$$D = D_0 \exp(-2\kappa a) \tag{2}$$

$$D_0 = \frac{16E(V_0 - E)}{V_0^2} \tag{3}$$

where $\kappa = ((2m(V_0 - E))/\hbar^2)^{1/2}$ is the decay constant, $\hbar = (h/2\pi)$ is the reduced Planck's constant, h is the Planck's constant, E is the kinetic energy of the electrons, V_0 is the barrier height, and a is the barrier length. D increases at elevated temperatures due to E increases with temperature, leading to an increase in the tunneling current and a decrease in the overall resistance of the film. Therefore, the synergistic response of the hole carrier number and the tunneling current when the temperature increased enabled the NiO/PVC resistive films to exhibit enhanced temperature-sensitive response characteristics. The resistance response of the sensor at ambient temperatures from 25 °C to 60 °C (40% relative humidity) is shown in Fig. 1(g). The temperature coefficient of resistance (TCR) is defined as

$$\text{TCR} = \frac{\Delta R / R_0}{\Delta T}. \tag{4}$$

The temperature sensitivity of the proposed sensor is −1.85%/°C ($R^2 = 0.966$), which is significantly higher than the reported NTC thermal temperature sensor for carbon-based materials (TCR ≈ −1%/°C) [31], [32].

The resistance of the temperature layer decreases exponentially with increasing temperature, showing the typical Arrhenius formula [33]

$$R = R_\infty e^{B/T} \tag{5}$$

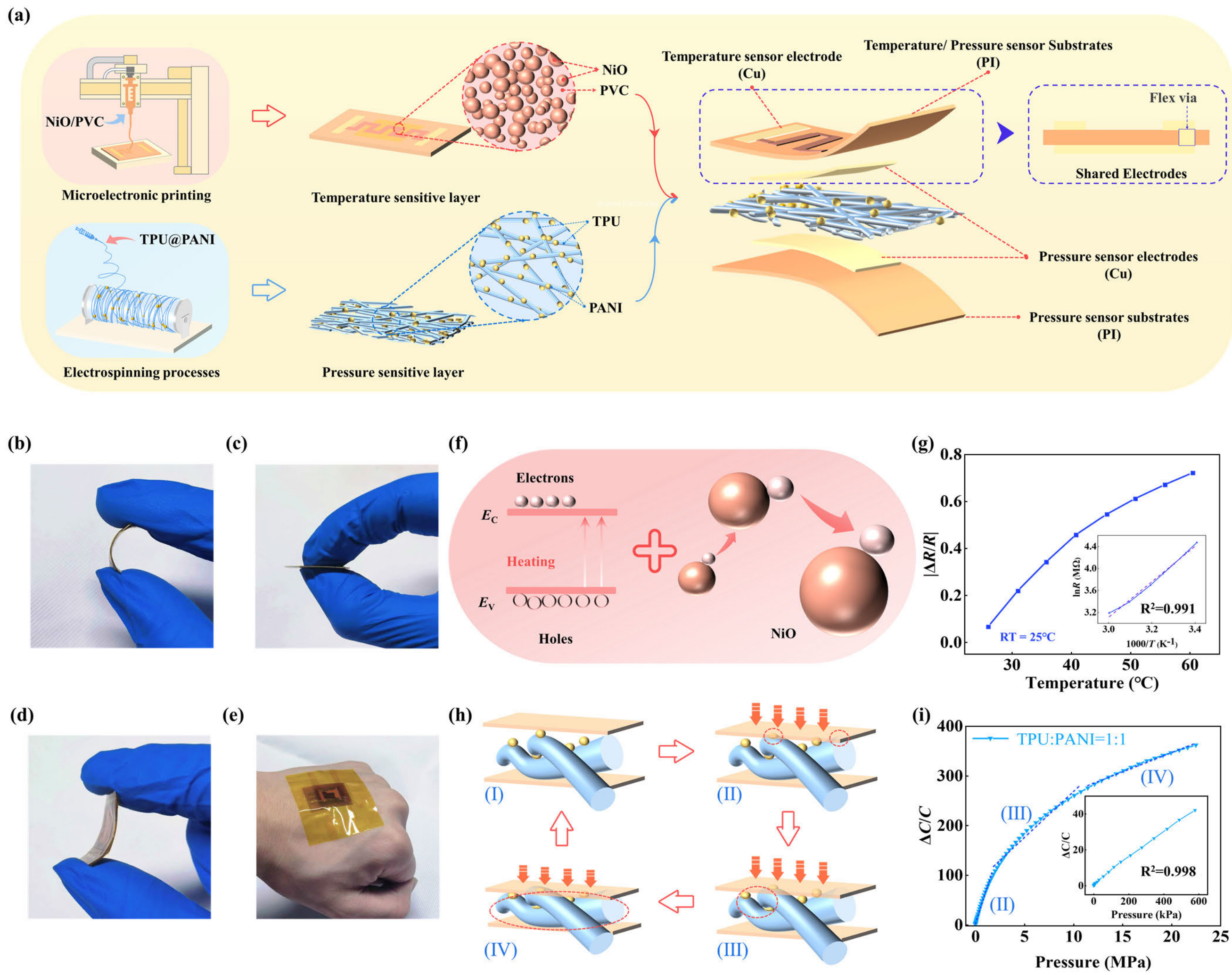

Fig. 1. (a) Schematic illustration of the dual-functional sensor's fabrication process and structure. (b)–(e) Optical images of the pressure-temperature sensor. Schematic illustration of the decoupled sensing mechanism for the dual-functional sensors when (f) temperature and (h) pressure are applied. Conceptual representation of integrated (g) temperature and (i) pressure sensing mechanisms employing the resistance and capacitance signal changes, respectively.

where R_∞ is the reference resistance of the sensor at infinite temperature, B is the Boltzmann's constant, which is only related to the properties of the material, a linear transformation of (5)

$$\ln R = \frac{B}{T} + \ln R_\infty. \tag{6}$$

As shown in the inset of Fig. 1(g), the linearly transformed horizontal and vertical coordinates are converted to 1000/T and lnR, respectively.

Fig. 1(h)-I displays the internal microstructure of the TPU@PANI-based pressure-sensitive fibrous membrane. The pressure response mechanism occurs through three distinct linear stages: First, when initial pressure is applied, it primarily acts on the "dots-knots" microstructures (Fig. 1(h)-II). These structures, characterized by their low modulus and high deformability, undergo rapid compression and flattening under minimal pressure, enabling an ultralow detection limitation (3 Pa). As air is expelled from the microstructures, the effective dielectric constant increases due to the higher relative permittivity of TPU@PANI compared to air. Second, pressure transfers to the membrane's porous architecture after complete microstructure compression, further elevating the effective dielectric constant (Fig. 1(h)-III). Finally, when all air is displaced, pressure acts directly on the TPU fibers. The membrane's high toughness limits deformation even under extreme pressures (>10 MPa), establishing the basis for an ultra-wide pressure range (Fig. 1(h)-IV). In this final stage, pressure primarily affects fiber layer spacing d and the effective dielectric constant, resulting in a comparatively lower relative capacitance change rate than previous stages. As illustrated in Fig. 1(i), the synergistic interaction between microstructures, air voids, and TPU fibers enables an exceptional 23 MPa pressure-capacitance response range. Significantly, the composite fiber membrane is thin enough to result in capacitance variations that are primarily caused by the effective dielectric constant with minimal effect of d, leading to the highly linear capacitance response in the inset of Fig. 1(i). The proposed pressure-sensitive layer exhibited outstanding linear responses ($R^2 = 0.998$) within the 0–600 kPa

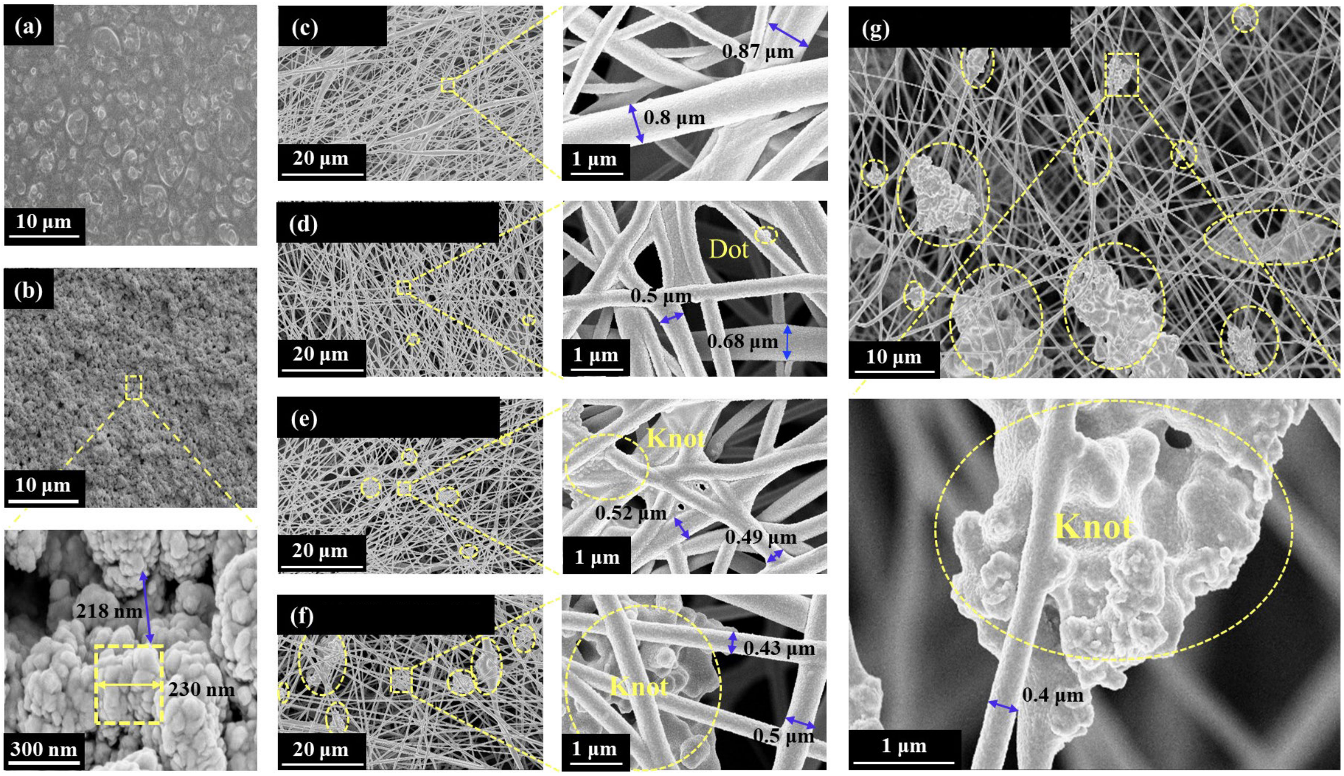

Fig. 2. SEM image of (a) PVC film, (b) NiO/PVC film, and (c) TPU film and corresponding localized enlargement. SEM images of TPU@PANI fiber membranes with different ratios PANI: TPU = (d) 9:1, (e) 3:1, (f) 2:1, and (g) 1:1, and corresponding localized enlargement.

pressure ranges. The temperature-sensitive layer is fabricated using a microelectronic printing process, which ensures its ultra-thin profile. This allows the hierarchical microstructure of the pressure-sensitive layer to effectively buffer the pressure applied to the temperature-sensitive layer. According to the parallel plate capacitor principle, the capacitance is determined by $C = \varepsilon * S/d$, where ε is the dielectric constant of the medium between the plates, S is the overlapping area of the capacitor plates, and d is the distance between the plates. Capacitive pressure sensors inherently exhibit temperature independence, as the spacing between the electrode plates, the dielectric constant, and the relative area are minimally affected by temperature changes, thereby resolving the issue of signal crosstalk.

B. Membrane Morphology

Fig. 2(a) and (b) show the microscopic topographies of pure PVC films and NiO/PVC hybrid films, and it can be concluded that NiO particles are uniformly distributed in the hybrid films. NiO nanoparticles measure approximately 230 nm in diameter, and individual particles are either directly connected or form gaps of hundreds of nanometers. The microscopic morphology and local magnification features of TPU@PANI composite fibrous membranes based on different ratios are shown in Fig. 2(c)–(g). The spun fiber membrane of pure TPU shows a smooth surface and no micro-structure as shown in Fig. 2(c). When a limited amount of PANI is doped (TPU: PANI = 9:1), the differences in viscosity and molecular chain structure between TPU and PANI lead to the "dots" appearing sporadically on the fiber membranes [Fig. 2(d)]. Further increasing the doping ratio to 3:1, "knots" with larger feature sizes are formed when "dots" on multiple fibers are clustered together [Fig. 2(e)]. The number of "dots" and "knots" in the 2:1 ratio gradually increases, and the characteristic size becomes larger [Fig. 2(f)]. The micro-structure feature size is largest when the doping ratio of TPU to PANI reaches 1:1 and the capacitive response of the pressure-sensitive layer achieves the maximum value [Fig. 2(g)]. The unique "dots" and "knots" micro-structure support an ultra-wide pressure range of the proposed dual-functional sensor.

C. Pressure and Temperature Sensing Performance

A series of static and dynamic experiments are carried out to characterize the sensing performance of the dual-functional sensors. The initial resistance of the temperature-sensitive layer of the dual-functional sensor is approximately 50 MΩ, and the initial capacitance of the pressure-sensitive layer is approximately 12 pF. NTC-based temperature-sensitive layer benefits from the current response of the carrier principle and generally possesses rapid response/recovery times. The temperature response of the sensors is generally consistent at temperatures from 35 °C to 60 °C [Fig. 3(a)]. Benefiting from the large surface area of the film, the temperature exchange between the temperature-sensitive layer and the environment is accelerated. Meanwhile, the thickness of the substrate is only 0.13 mm, which facilitates the heat dissipation of the sensor and accelerates its recovery time. The response time is 1 s and the recovery time is 16.9 s [Fig. 3(b)], which is much faster than the current commercial platinum (Pt) temperature sensors (about 5 min). Fig. 3(c) demonstrates the electrical

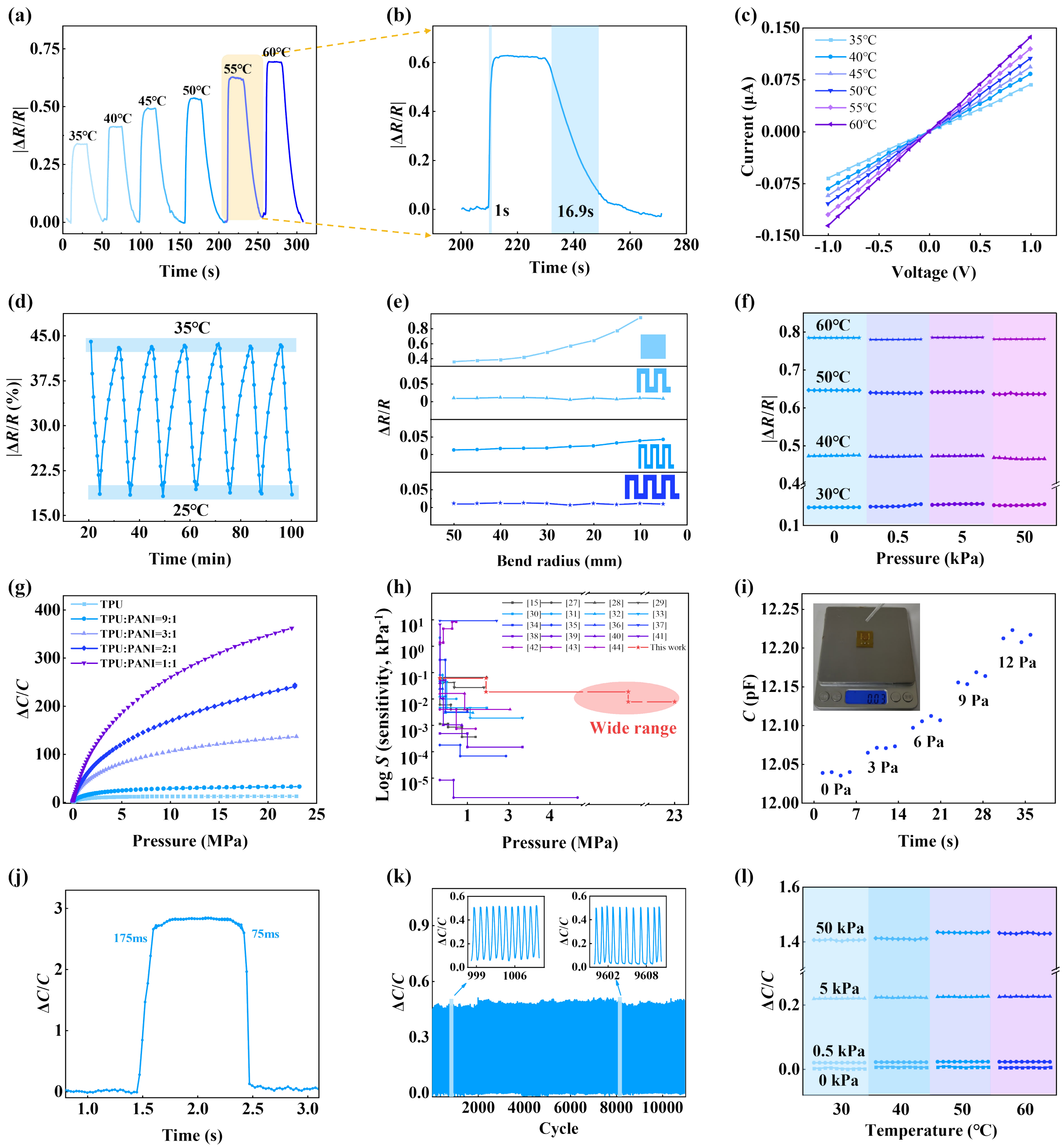

Fig. 3. Performance in temperature-pressure sensing by the sensor. (a) Resistance changes of the sensor at different temperatures. (b) $|\Delta R/R|$ and recovery time of the temperature-sensitive layer. (c) $I-V$ curves of the temperature-sensitive layer measured under various temperatures. (d) $\Delta R/R$ during six temperature cycling response from 25 °C to 35 °C. (e) $\Delta R/R$ under temperature-sensitive layers of different shapes and sizes. (f) Dependence of $\Delta R/R_0$ on pressure. (g) Capacitance values of the pressure-sensitive layers at different doping ratios for various pressures. (h) Comparison of pressure sensitivity (S) and sensor detection range with other literature (TPU: PANI = 1:1). (i) $\Delta Cc/C$ of the pressure-sensitive layer at subtle pressures. (j) Response/recovery time of the pressure-sensitive layer at 50 kPa. (k) Stability of the pressure-sensitive layer across 10 000 cycles at a pressure of 10 kPa, the inset shows the local enlargement. (l) Dependence of $\Delta C/C$ on temperature.

characteristics of the temperature-sensitive layer in the range of 35 °C–60 °C. The current response is obtained at scanning voltages from −1 to 1 V (0.1 V pitch), and each of the I–V curves exhibits great linearity. The slope of the I–V curves increases with temperature, showing a typical semiconductor NTC resistance response.

Cycling stability is a critical factor in determining the service life and reliability of the sensor. As shown in Fig. 3(d), the sensor exhibits consistent response characteristics during temperature cycling between 25 °C and 35 °C, also demonstrating its ability to achieve a reliable temperature response during both heating and cooling processes. We characterized the sensor's temperature hysteresis as shown in Fig. S1 (Supporting Information), and the results showed that the temperature hysteresis error was reduced to 1% over the operating temperature range of 25 °C–60 °C.

However, the deformation that inevitably occurs during the measurement process increases the spacing between the NiO particles, which affects the electron transfer efficiency and increases the film resistance. Different shapes of temperature-sensitive layers are designed to clarify the effect of shape on anti-bending properties. As illustrated in Fig. 3(e), the resistance change of the square-sensitive film is more pronounced within a bending radius range of 10–50 mm, with the resistance change reaching up to 100% at a bending radius of 10 mm. In contrast, the serpentine structure not only concentrates tensile stresses at the connection corners, thereby minimizing the impact of deformation ON resistance, but also increases the surface area exposed to air, leading to an enhanced temperature response. Compared to square thermistors, serpentine thermistors demonstrate greater sensitivity to small-area heating, higher signal-to-noise ratios (SNRs), and superior anti-bending performance [27]. Additionally, the wide-linewidth serpentine resistor achieves a lower initial resistance, which is particularly advantageous given that the initial resistance of semiconductor materials typically ranges in the order of MΩ. This reduction in initial resistance helps lower the design cost and power consumption of readout circuits. All three serpentine structures exhibit excellent anti-bending characteristics across a bending radius range of 5–50 mm, with a maximum resistance change of less than 4%. Notably, the serpentine structure with a 1.5 mm linewidth maintains a resistance change of less than 1% even at a bending radius of 5 mm. Fig. 3(f) shows that the temperature-sensitive layer is subjected to different pressures (0, 0.5, 5, and 50 kPa) at temperatures of 30 °C, 40 °C, 50 °C, and 60 °C and achieves insensitivity to pressure (pressure-induced resistance change not exceeding 1%) for a sustained period (1 min).

Composite fiber membranes with different micro-morphological structures were successfully prepared by changing the relative proportions of TPU and PANI. As shown in Fig. 3(g), the capacitive response of the pressure-sensitive layer increased with the further increase of PANI content. The sensitivity S of the flexible capacitive pressure sensor can be defined as

$$S = \frac{\Delta C / C}{\Delta P}. \tag{7}$$

ΔC is the capacitance change, C is the initial capacitance, and ΔP is the applied pressure range. Considering both linearity and sensitivity, the pressure-sensitive layer exhibits strong linearity ($R_1^2 = 0.991$, $R_2^2 = 0.975$, and $R_3^2 = 0.991$) across pressures of 0–1675 kPa, 1675–11 480 kPa, and 11.48–23 MPa with the sensitivities of $S_1 = 0.0611$ kPa^{-1}, $S_2 = 0.0185$ kPa^{-1}, and $S_3 = 0.00776$ kPa^{-1}. The sensitivity degradation of the pressure-sensitive layer does not exceed ten times in the ultra-wide range (11.48–23 MPa). The sensitivity is successfully increased up to 11 times compared to pure TPU membranes by controlling the ratio of PANI to TPU to modulate the micro-structure (pressure sensitivity of pure TPU fiber membranes is 0.00527 kPa^{-1} in the pressure range of 0–1675 kPa). Most flexible capacitive pressure sensors have less than 2 MPa range, as shown in Fig. 3(h). The flexible capacitive pressure-sensitive layer based on the TPU@PANI designed in this article extends the maximum measurable pressure to 23 MPa based on ensuring an ultralow pressure limit detection (3 Pa), which has never been reported in the literature before for richer application scenarios. We have included in the Supporting Information (Fig. S2) a comparison of the capacitance versus applied pressure for dual-function sensors, along with a magnified view of the local region. These supplementary figures further illustrate the response characteristics of the proposed sensor in both low- and high-pressure ranges, while emphasizing its unique advantages in ultra-wide-range detection.

Deionized water droplets were used as the pressure source for the low-pressure detection limit test. A single droplet of deionized water (approximately 0.3 g) with a contact area of about 1 cm^2 exerts a pressure of approximately 3 Pa on the sensor. As the number of droplets increases, the contact area remains almost unchanged due to the surface tension of water, while the pressure increases proportionally with the weight of the droplets. Ultimately, four droplets generate a pressure of about 12 Pa. As shown in Fig. 3(i), four measurements are taken in each case to ensure the accuracy of the results. All four measurements taken under each pressure condition show similar levels with only minor fluctuations caused by noise in the measuring instrument. The response and recovery times at 50 kPa are recorded by placing 500 g of weights on the pressure-sensitive layer (maintained for 1 s) with a response time of 175 ms. In contrast, the recovery time does not exceed 75 ms [Fig. 3(j)]. The fast response and recovery performance of pressure sensing is attributed to the TPU body in the fiber membrane. The high strength and toughness of the elastic TPU fibers provide a fast response to the compression and recovery of the pressure-sensitive layer. Three cycles at bending angles of 15°, 30°, 45°, 60°, 75°, and 90° are shown in Fig. S3 (Support Information). The response values are essentially similar at the same angles, and the capacitive response returns to the unbent value after each bending recovery, showing excellent bending stability even at 90° bending, which demonstrates the high flexibility and robustness of the pressure-sensitive layer. The sensor is tested for 10 000 pressure loading-unloading cycles (at 10 kPa pressure), as shown in Fig. 3(k). The capacitive response of the sensor demonstrated consistent stability throughout the process. The inset presents the capacitive response values of the sensor for 11 cycles at the beginning and end stages, indicating that the sensor's response value did not degrade significantly over the 10 000 cycles. One of the most critical properties of temperature-pressure sensors is the ability to avoid signals interfering with each other, and the insensitivity of temperature sensing under pressure conditions has been demonstrated in Fig. 3(f). The capacitive response is observed by loading different pressure conditions (0, 0.5, 5, 50 kPa) and then placing them at 30 °C, 40 °C, 50 °C, and 60 °C, as shown in Fig. 3(l).

The dual-functional sensor exhibits slight fluctuations in resistance while maintaining a constant temperature, but the relative resistance change rate remains stable over a certain period (1 min), as shown in Fig. S4 (Supporting Information).

The temperature response of the pressure sensing is stable at a high pressure of 50 kPa. The temperature sensitivity coefficient of pressure ($S_{P,T}$) represents the influence of temperature changes on pressure measurements and is typically defined as

$$S_{P,T} = \Delta P / \Delta T \tag{8}$$

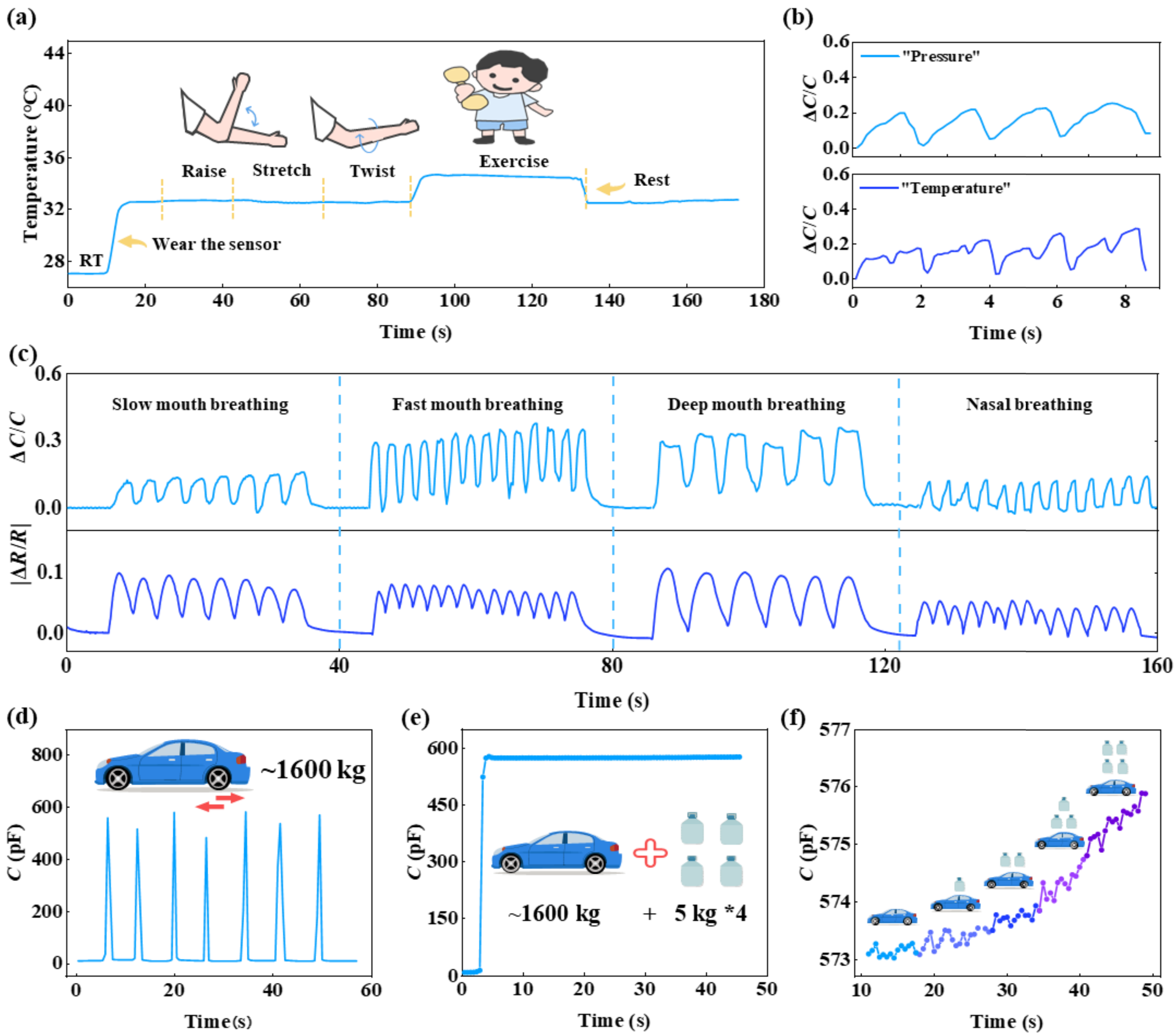

Fig. 4. Application of dual-functional sensor in wearable electronic devices. (a) Temperature response to human skin in motion. (b) Recognition of different breathing patterns. (d) Response of the pressure sensor under repetitive loading from a ∼1600 kg fully loaded car. (e) and (f) Sensing of the pressure sensor when four 5 kg buckets get on the car.

where ΔP is the change in pressure (in kPa) and ΔT is the change in temperature (in °C), the same pressure is applied at different temperatures. As demonstrated in Fig. S5 (Supporting Information), the temperature sensitivity coefficient of pressure under 50 kPa is determined to be 0.036 kPa/°C, with pressure fluctuations remaining below 1 kPa. This value indicates that temperature has a minimal influence on pressure measurements, confirming the excellent temperature-pressure decoupling performance of the sensor.

Table I (Supporting Information) summarizes the key performance of representative flexible temperature-pressure sensors in the last five years. The NiO/TPU@PANI flexible temperature-pressure sensor proposed in this work achieves the key performance of signal-independent decoupling. The dual-functional sensor not only achieves high temperature sensing sensitivity and ultralow pressure limit detection but also demonstrates high linearity (>0.99) over a wide linear sensing range (0–1675 kPa and 11.48–23 MPa). The maximum range of pressure sensing is up to 23 MPa, which is the highest level among the reported papers. The dual-function sensor encapsulated with PI exhibits minimal output changes when fingertips, weights, or beakers approach, while maintaining excellent low-pressure detection capability and response characteristics after proximity, as evidenced by the proximity test results (Fig. S6 in Supporting Information).

D. Applications in Wearable Electronic Devices

Benefiting from the high curvature fit of the flexible sensor, the temperature monitoring can accurately reflect the changes in human body temperature during movement, and the pressure sensor can detect various movement states and limb movements. The sensor response rises rapidly to 32.7 °C (body surface temperature) when the sensor is placed on the arm as shown in Fig. 4(a), the temperature response of the

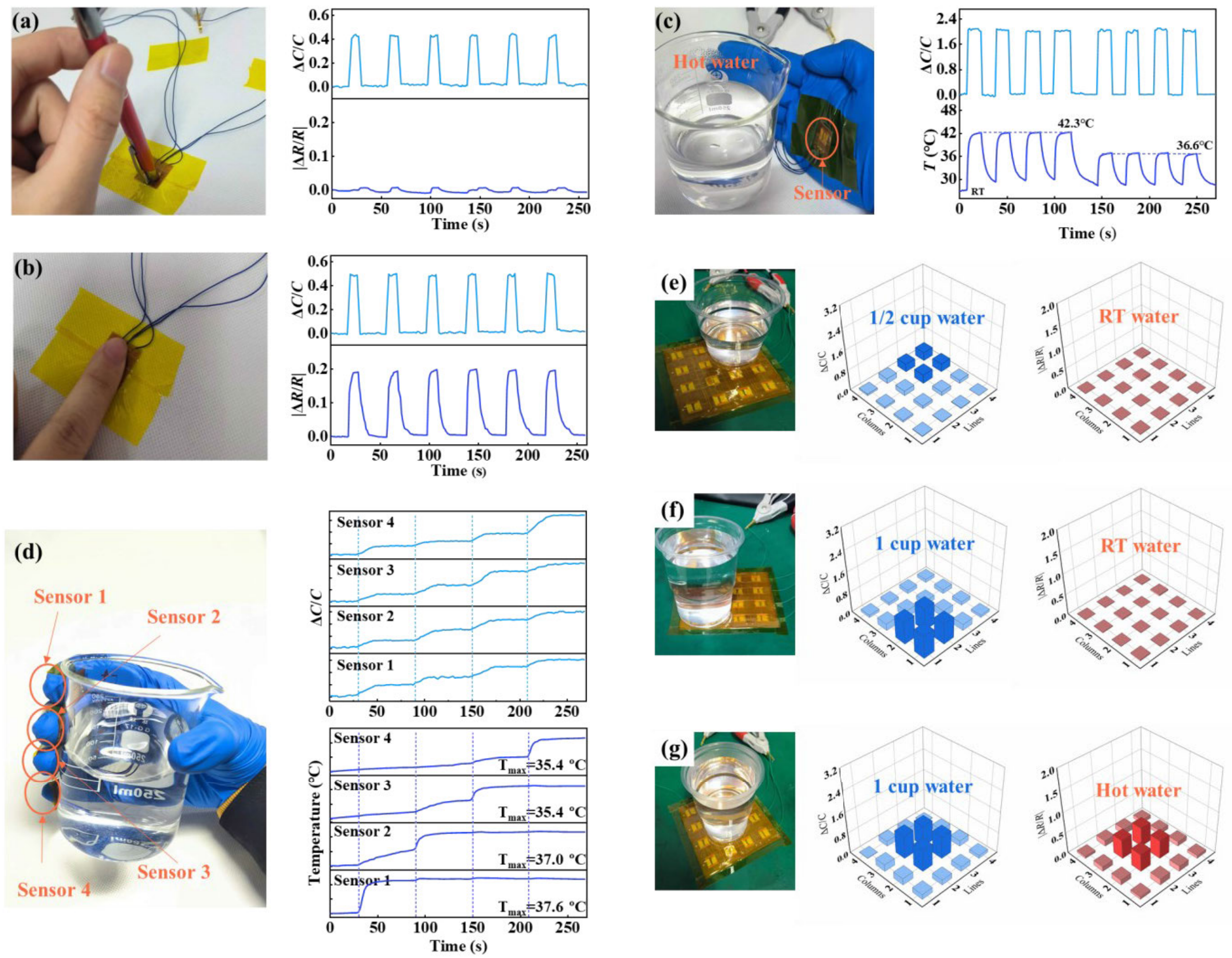

Fig. 5. Flexible sensor array for spatial sensing of pressure and temperature. Sensor response to loading-unloading (a) pen and (b) finger tactile and temperature stimulation cycles. (c) Temperature and pressure response to contact-separation of hot water cup at different temperatures. (d) Temperature-pressure gradient field sensing. Dual-functional mode array sensing applications [(e) 1/2 cup RT water, (f) 1 cup RT water, and (g) 1 cup hot water].

sensor remains almost constant when lifting, stretching, and twisting the arm, indicating that multiple dynamic processes do not interfere with the temperature response of the sensor (bending, pressure insensitivity). Later, the body surface temperature increases to 35 °C and maintains a certain level during exercise. When the movement stops, the temperature response returns to the body temperature of the previous non-movement moment. The capacitive output characteristics of the sensor applied to the throat for the words "temperature" and "pressure" are different, as seen in Fig. 4(b). The individual capacitive response has two peaks when recognizing the more syllabic "temperature" while the less syllabic "pressure" has only one response peak. As illustrated in Fig. S7 (Supporting Information), the sensors are attached to the knee, palm, and corner of the eye to detect pressure responses to body movements. The sensor consistently achieves the same response value during each bending cycle and can return to its initial response state once the bending motion is ceased. The dual-functional sensor can recognize different breathing states by accurately measuring the temperature and air pressure of the exhaled gas. Fig. 4(c) illustrates the pressure and temperature responses of the sensor for different mouth breathing and nasal breathing modes while wearing a mask. The temperature variation range of nasal breathing (27.9 °C–29.5 °C) is lower than mouth breathing (28.0 °C–31.1 °C). When the airflow pressures of nasal and oral respiration are essentially similar, supplemental temperature monitoring can differentiate between oral and nasal respiration. The temperature or pressure responses in different breathing modes are relatively close in certain cases, e.g., the temperature responses of slow mouth breathing and deep mouth breathing are nearly identical, thus single-mode recognition might lead to misidentification. Complementary monitoring between pressure and temperature allows for accurate differentiation of various breathing patterns, including slow mouth breathing, rapid mouth breathing, deep mouth breathing, and nasal breathing. Therefore, the dual-functional sensor can realize the recognition of multiple complex respiratory states that are difficult to achieve with single-mode sensors, which is highly demanded in flexible medical devices. This result shows the potential of the proposed sensor for medical applications, where accurate recognition of breathing patterns could provide early warning of respiratory distress for asthma patients and children. High-pressure-resistant pressure sensors play a critical role in various extreme environments, particularly in applications such as structural health monitoring of bridges and load detection in heavy machinery. These sensors must not only endure extremely high pressures but also maintain high accuracy and stability under complex conditions. Fig. 4(d) depicts a scenario in which a fully loaded car weighing ~1600 kg repeatedly passes over the dual-function sensor. The pressure sensor is positioned beneath one of the car's wheels, and as the car drives over it, the sensor's output capacitance rapidly increases and then recovers. Despite being subjected to multiple compressions, the sensor consistently maintains stable sensing performance, demonstrating its remarkable durability and reliability. When four water barrels with the weight of 5 kg are sequentially loaded onto the car, the dual-function sensor successfully detects these pressure changes. Fig. 4(e) and (f) displays the corresponding capacitance variation curve, clearly indicating that the proposed sensor device can operate stably under high-pressure conditions while also being capable of sensitively capturing relatively small pressure changes. Fig. S8 (Supporting Information) illustrates a real-time communication application based on the international standard Morse code table. The Morse code of letters "A," "B," and "C," numbers "1," "2," and "3," and the phrase "I LOVE SEU" is obtained by pressing the sensor surface, which can be helpful for people with limited muscle function.

To verify that the sensor can sense and decouple temperature and pressure stimuli simultaneously and independently, we designed a series of contact loading-unloading experiments at room temperature (25 °C). The sensor can detect both the capacitive change caused by pressure and the thermistor response caused by temperature when a finger touches it [Fig. 5(a)]. Only the pressure-induced capacitive response exists when touching the sensor with the pen, and the temperature response disappears because the pen and the sensor are at the same room temperature [Fig. 5(b)]. The dual-functional sensor is mounted on an experimental glove and the contact separation cycle experiment is performed on beakers containing hot water of different temperatures, as shown in Fig. 5(c). The pressure response of the sensor does not change much when in contact with hot water of different temperatures. Multiple parallel dual-functional sensors can detect both temperature and pressure gradient field responses. Four sensors are mounted on the little, ring, middle, and index finger as shown in Fig. 5(d). Then the beaker is filled with 40 °C water in four stages, ensuring that the level of the beaker passes over the sensors on the little, ring, middle, and index fingers in that order (held for 1 min after each stage). Each sensor shows accurate gradient sensing for both pressure and temperature. The capacitive response values of the sensors in all four positions increase with the amount of water filled because the total weight of the beaker increases. It is worth noting that as the hot water heats the beaker walls and steam evaporates upward, the sensors that have not yet contacted the hot water surface also show a temperature response, and the closer they are to the hot water surface the greater the capacitive response of the sensors. Sensor 3 located on the index finger shows a more pronounced change in overall temperature response after the third injection of hot water and quickly reaches a level consistent with the other sensors after the last injection of hot water. Customized FPC electrode arrays are used to prepare 4×4 temperature-pressure array sensors. Different masses and temperatures of water are placed at different locations of the array to measure its spatial resolving ability, as shown in Fig. 5(e)–(g). Half a cup of water at room temperature is placed at the four sensing sites in the upper right corner, and the results show a large pressure capacitance response and no significant temperature response. The capacitive response of the surrounding sensing sites spreads outward and decays around the pressure center because the upper electrodes of the array are constructed on the same PI substrate. Subsequently, a full cup of water is placed in the lower left corner, and the capacitive response value of the sensing site is significantly greater than half a cup of water. Finally, a cup of hot water is placed in the center, producing a significant thermistor response. The thermistor response is present at all locations on the array due to the temperature field, with the response value decaying by diffusion from the temperature field to the surroundings. The array sensors not only possess spatial resolution under stimulation of temperature and pressure but also have no crosstalk between the two response signals, indicating that NiO/TPU@PANI flexible dual-functional sensor has a broad application prospect in human physical signal monitoring, information communication, electronic skin.

III. Conclusion

In this article, an intrinsically integrated hierarchical flexible temperature-pressure sensor is fabricated using microelectronic printing and electrostatic spinning processes. Independent NiO resistive temperature-sensitive and TPU@PANI capacitive pressure-sensitive sensing systems with hierarchical sandwich structures are developed. The unique microstructure constructed by adjusting the doping concentration of PANI effectively realizes the hierarchical pressure sensing to obtain an ultra-wide pressure range of 23 MPa, high linearity values of 0.998 and 0.991 in ranges of 0–580 kPa and 10–23 MPa, an ultralow pressure detection limit of 3 Pa. Meanwhile, the hierarchical micro-structure buffers the pressure acting on the temperature-sensitive layer to solve the signal crosstalk. The dual-functional sensor has a high sensitivity of −1.85%/°C over the range of 25 °C–60 °C, a fast response time of 1 s, and low hysteresis characteristics. These results provide a foundation for the development of integrated multifunctional sensors and create engineering opportunities for wearable health monitoring and human–machine interface applications.

IV. Methods

NiO nanoparticles with 99.5% purity and particle size less than 30 nm were purchased from Jiuding Chemical Technology Inc. (Shanghai, China). PVC was obtained from Aladdin Biochemical Technology Inc. (Shanghai, China). N, N-DMF was purchased from Maclean's Biochemical Technology Inc. (Shanghai, China). Acetone (CH3COCH) with 99.7% purity was purchased from Nanjing Reagent Inc. (Nanjing, China). TPU was purchased from Bayer Biotechnology Inc. (Germany), and PANI was purchased from Maclean's Biochemical Technology Inc. (Shanghai, China). All materials were used as-received without further purification.

Fabrication of Temperature-Sensitive Film: Microelectronic printer (DB-100) was purchased from Prtronic Inc. (Shanghai, China). As shown in Fig. 1(a), 0.35 g of NiO and 0.05 g of PVC were dissolved in 1 mL of DMF solvent and stirred at room temperature for 3 h with the rotational speed set to 1000 r/min. The mixed solution was transferred into a syringe of a microelectronic printer with a needle size of 0.34 mm, a dispensing speed of 1.5 mm/s, a dispensing air pressure of 37 kPa, and a substrate preheated at 60 °C. The temperature-sensitive pattern layer was printed on the ethanol-cleaned customized flexible circuit board (FPC). The printed temperature-sensitive layer was placed in an oven and dried for 1 h at 60 °C.

Fabrication of Pressure-Sensitive Film: Electrostatic spinning machine (MSK-NFES-1U) was purchased from Kejing Material Technology Inc. (Hefei, China). As shown in Fig. 1(a), 0.6 g of TPU was mixed with 3.1 mL of acetone and 1.9 mL of DMF solution. The solution was stirred at 30 °C for 0.5 h at a speed of 1000 r/min. 0.6 g of PANI was added to the mixed solution and stirring was continued for 2 h to obtain a spinning solution with TPU: PANI = 1:1. Four different ratios of spinning solution were additionally configured to compare the pressure performance (TPU: PANI = 2:1, 3:1, 9:1, and pure TPU). The spinning solution was sequentially transferred to the spinning syringe at a spinning speed of 1 mL/h, a syringe diameter of 10 mm, a spinning voltage of 15 kV, and a spinning needle with an inner diameter of 0.51 mm. The drum was placed 15 cm away from the spinning needle and the rotational speed was set to 800 r/min. The foils covered with the spinning fiber film were removed from the drum and placed into an oven to be dried at 60 °C for 1 h and then peeled off the fiber film.

Dual-Functional Sensors Testing Principle: A MARK 10 mechanical testing machine, equipped with an ESM303 force-measuring platform and SERICE 5 digital force-measuring instrument (with 1–1000 mm/min load rate) and standard weights, were used to test the tensile mechanics of the dual-functional sensors by applying pressure on the sensor. The heating platform (V-1010) was purchased from Dongguan vectech Automation Technology Inc. (China), and the constant temperature and humidity chamber (C-340) was purchased from Weiss Technik International Inc (China). for testing the temperature response of the dual-function sensor. The sensor electrodes were connected to the semiconductor parameter analyzer 4200A-SCS (Keithley, America) with 5 ns sampling rate, LCR digital bridge (TH2826A, purchased from Changzhou Tonghui Electronics Inc.), and LCR-6200 (GWINSTEK, Taiwan) with 25 ms sampling rate) for electrical testing and outputting the resistance/capacitance signals of the dual-functional sensors.

References

[1] X. Zhang et al., "Flexible pressure sensors with combined spraying and self-diffusion of carbon nanotubes," *ACS Appl. Mater. Interfaces*, vol. 14, no. 33, pp. 38409–38420, Aug. 2022.

[2] W. Cheng et al., "Flexible pressure sensor with high sensitivity and low hysteresis based on a hierarchically microstructured electrode," *IEEE Electron Device Lett.*, vol. 39, no. 2, pp. 288–291, Feb. 2018.

[3] Y. Jeong, J. Park, J. Lee, K. Kim, and I. Park, "Ultrathin, biocompatible, and flexible pressure sensor with a wide pressure range and its biomedical application," *ACS Sensors*, vol. 5, no. 2, pp. 481–489, Feb. 2020.

[4] L. Dan and A. L. Elias, "Flexible and stretchable temperature sensors fabricated using solution-processable conductive polymer composites," *Adv. Healthcare Mater.*, vol. 9, no. 16, Aug. 2020, Art. no. 2000380.

[5] T. Xu et al., "Application and optimization of stiffness abruption structures for pressure sensors with high sensitivity and anti-overload ability," *Sensors*, vol. 17, no. 9, p. 1965, Aug. 2017.

[6] Z. Xu et al., "An SOI-structured piezoresistive differential pressure sensor with high performance," *Micromachines*, vol. 13, no. 12, p. 2250, Dec. 2022.

[7] M. Basov, "Research of MEMS pressure sensor stability with PDA-NFL circuit," *IEEE Sensors J.*, vol. 24, no. 21, pp. 34083–34090, May 2024.

[8] M. Basov, "Research of long-term stability of high-sensitivity piezoresistive pressure sensors for ultralow differential pressures," *IEEE Sensors J.*, vol. 24, no. 22, pp. 36443–36450, Aug. 2024.

[9] Y. Liu, X. Jiang, H. Yang, H. Qin, and W. Wang, "Structural engineering in piezoresistive micropressure sensors: A focused review," *Micromachines*, vol. 14, no. 8, p. 1507, Jul. 2023.

[10] Y. Yuan et al., "A piezoelectric MEMS resonant temperature sensor with 10-μk resolution and 0.06-PJK2 resolution FOM," in *Proc. IEEE 37th Int. Conf. Micro Electro Mech. Syst. (MEMS)*, Austin, TX, USA, Jan. 2024, pp. 983–986.

[11] S. Ji, P. Akhkandi, Y. Qi, R. Abdolvand, and H. M. Lavasani, "A wide-dynamic range (-40°C to 180 °C) active wireless MEMS temperature sensor with 7m °C sensitivity," *IEEE Sensors J.*, vol. 23, no. 9, pp. 9194–9203, May 2023.

[12] S. Wang et al., "Flexible optoelectronic multimodal proximity/pressure/temperature sensors with low signal interference," *Adv. Mater.*, vol. 35, no. 49, Dec. 2023, Art. no. 2304701.

[13] J. Xu et al., "Stretchable, adhesive, and bioinspired visual electronic skin with strain/temperature/pressure multimodal non-interference sensing," *ACS Appl. Mater. Interfaces*, vol. 15, no. 28, pp. 33774–33783, 2023.

[14] H. Xiao et al., "Dual mode strain-temperature sensor with high stimuli discriminability and resolution for smart wearables," *Adv. Funct. Mater.*, vol. 33, no. 16, Apr. 2023, Art. no. 2214907.

[15] F. Li et al., "Printable and stretchable temperature-strain dual-sensing nanocomposite with high sensitivity and perfect stimulus discriminability," *Nano Lett.*, vol. 20, no. 8, pp. 6176–6184, Aug. 2020.

[16] F. Yin et al., "A waterproof and breathable cotton/rGO/CNT composite for constructing a layer-by-layer structured multifunctional flexible sensor," *Nano Res.*, vol. 15, no. 10, pp. 9341–9351, Oct. 2022.

[17] S. Wang et al., "All-nanofiber iontronic sensor with multiple sensory capabilities for wearable electronics," *Adv. Mater. Technol.*, vol. 9, no. 9, May 2024, Art. no. 2301791.

[18] H. Zhu, H. Luo, M. Cai, and J. Song, "A multifunctional flexible tactile sensor based on resistive effect for simultaneous sensing of pressure and temperature," *Adv. Sci.*, vol. 11, no. 6, Feb. 2024, Art. no. 2307693.

[19] Y. Wang et al., "High-sensitivity self-powered temperature/pressure sensor based on flexible bi-te thermoelectric film and porous microconed elastomer," *J. Mater. Sci. Technol.*, vol. 103, pp. 1–7, Mar. 2022.

[20] Y. Li et al., "Mutually noninterfering flexible pressure-temperature dual-modal sensors based on conductive metal-organic framework for electronic skin," *ACS Nano*, vol. 16, no. 1, pp. 473–484, 2022.

[21] G. Y. Bae et al., "Pressure/Temperature sensing bimodal electronic skin with stimulus discriminability and linear sensitivity," *Adv. Mater.*, vol. 30, no. 43, Oct. 2018, Art. no. 1803388.

[22] P. Zhu, Y. Wang, M. Sheng, Y. Wang, Y. Yu, and Y. Deng, "A flexible active dual-parameter sensor for sensitive temperature and physiological signal monitoring via integrating thermoelectric and piezoelectric conversion," *J. Mater. Chem. A*, vol. 7, no. 14, pp. 8258–8267, 2019.

[23] W. Yang et al., "Multifunctional soft robotic finger based on a nanoscale flexible temperature-pressure tactile sensor for material recognition," *ACS Appl. Mater. Interfaces*, vol. 13, no. 46, pp. 55756–55765, Nov. 2021.

[24] K. L. Cao et al., "Beyond skin pressure sensing 3D printed laminated graphene pressure sensing material," *Adv. Funct. Mater.*, vol. 32, no. 28, 2022, Art. no. 2202360.

[25] C. Ye et al., "Design and fabrication of silk templated electronic yarns and applications in multifunctional textiles," *Matter*, vol. 1, no. 5, pp. 1411–1425, Nov. 2019.

[26] S. Veeralingam and S. Badhulika, "Bi_2S_3/PVDF/Ppy-based freestanding, wearable, transient nanomembrane for ultrasensitive pressure, strain, and temperature sensing," *ACS Appl. Bio Mater.*, vol. 4, no. 1, pp. 14–23, Jan. 2021.
[27] H. Luo, G. Pang, K. Xu, Z. Ye, H. Yang, and G. Yang, "A fully printed flexible sensor sheet for simultaneous proximity-pressure-temperature detection," *Adv. Mater. Technol.*, vol. 9, no. 2, Jan. 2024, Art. no. 2100616.
[28] J. Shin et al., "Sensitive wearable temperature sensor with seamless monolithic integration," *Adv. Mater.*, vol. 32, no. 2, Jan. 2020, Art. no. 1905527.
[29] R. Deng et al., "X-ray photoelectron spectroscopy measurement of n-ZnO/p-NiO heterostructure valence-band offset," *Appl. Phys. Lett.*, vol. 94, no. 2, p. 4719, Jan. 2009.
[30] Y. Xiao, S. Jiang, Y. Li, and W. Zhang, "Screen-printed flexible negative temperature coefficient temperature sensor based on polyvinyl chloride/carbon black composites," *Smart Mater. Struct.*, vol. 30, no. 2, Feb. 2021, Art. no. 025035.
[31] S. Pradhan and V. K. Yadavalli, "Photolithographically printed flexible silk/PEDOT: PSS temperature sensors," *ACS Appl. Electron. Mater.*, vol. 3, no. 1, pp. 21–29, Jan. 2021.
[32] Z. Liu et al., "Tuned transport behavior of the IPA-treated PEDOT: PSS flexible temperature sensor via screen printing," *J. Electron. Mater.*, vol. 50, no. 4, pp. 2356–2364, Apr. 2021.
[33] A. Feteira, "Negative temperature coefficient resistance (NTCR) ceramic thermistors: An industrial perspective," *J. Amer. Ceram. Soc.*, vol. 92, pp. 967–983, May 2009.
[34] S. Zhang, F. Wang, H. Peng, J. Yan, and G. Pan, "Flexible highly sensitive pressure sensor based on ionic liquid gel film," *ACS Omega*, vol. 3, no. 3, pp. 3014–3021, Mar. 2018.
[35] S. W. Park, P. S. Das, and J. Y. Park, "Development of wearable and flexible insole type capacitive pressure sensor for continuous gait signal analysis," *Organic Electron.*, vol. 53, pp. 213–220, Feb. 2018.
[36] W. Li et al., "A porous and air gap elastomeric dielectric layer for wearable capacitive pressure sensor with high sensitivity and a wide detection range," *J. Mater. Chem. C*, vol. 8, no. 33, pp. 11468–11476, Aug. 2020.
[37] B. Ji et al., "Gradient architecture-enabled capacitive tactile sensor with high sensitivity and ultrabroad linearity range," *Small*, vol. 17, no. 43, Oct. 2021, Art. no. 2103312.
[38] K. Nie et al., "Anisotropic, flexible wood hydrogels and wrinkled, electrodeposited film electrodes for highly sensitive, wide-range pressure sensing," *ACS Appl. Mater. Interfaces*, vol. 12, no. 38, pp. 43024–43031, Sep. 2020.
[39] J. Wu et al., "Rational design of flexible capacitive sensors with highly linear response over a broad pressure sensing range," *Nanoscale*, vol. 12, no. 41, pp. 21198–21206, Oct. 2020.
[40] Z. Liu et al., "Natural bamboo leaves as dielectric layers for flexible capacitive pressure sensors with adjustable sensitivity and a broad detection range," *RSC Adv.*, vol. 11, no. 28, pp. 17291–17300, 2021.
[41] H. Yu et al., "Wide-range flexible capacitive pressure sensors based on dielectrics with various porosity," *Micromachines*, vol. 13, no. 10, p. 1588, Sep. 2022.
[42] Z. Zhao et al., "Bioinspired hierarchical structure for an ultrawide-range multifunctional flexible sensor using porous expandable polyethylene/loofah-like polyurethane sponge material," *Adv. Intell. Syst.*, vol. 5, no. 1, Jan. 2023, Art. no. 2200295.
[43] S. Masihi et al., "Highly sensitive porous PDMS-based capacitive pressure sensors fabricated on fabric platform for wearable applications," *ACS Sensors*, vol. 6, no. 3, pp. 938–949, Mar. 2021.
[44] S. Kim, Y. Jung, S. Oh, H. Moon, and H. Lim, "Parasitic capacitance-free flexible tactile sensor with a real-contact trigger," *Soft Robot.*, vol. 9, no. 1, pp. 119–127, Feb. 2022.
[45] Y. Ko, C. C. Vu, and J. Kim, "Carbonized cotton fabric-based flexible capacitive pressure sensor using a porous dielectric layer with tilted air gaps," *Sensors*, vol. 21, no. 11, p. 3895, Jun. 2021.
[46] Y. Xiao et al., "Multilayer double-sided microstructured flexible iontronic pressure sensor with a record-wide linear working range," *ACS Sensors*, vol. 6, no. 5, pp. 1785–1795, May 2021.
[47] D. Yoo, D.-J. Won, W. Cho, J. Lim, and J. Kim, "Double side electromagnetic interference-shielded bending-insensitive capacitive-type flexible touch sensor with linear response over a wide detection range," *Adv. Mater. Technol.*, vol. 6, no. 11, Nov. 2021, Art. no. 2100358.
[48] Q. He et al., "Flexible conductivity-temperature-depth-strain (CTDS) sensor based on a CNT/PDMS bottom electrode for underwater sensing," *Flexible Printed Electron.*, vol. 7, no. 4, Dec. 2022, Art. no. 045002.
[49] L. Yang, X. Liu, Y. Xiao, Y. Zhang, G. Zhang, and Y. Wang, "3D printing of carbon nanotube (CNT)/Thermoplastic polyurethane (TPU) functional composites and preparation of highly sensitive, wide-range detectable, and flexible capacitive sensor dielectric layers via fused deposition modeling (FDM)," *Adv. Mater. Technol.*, vol. 8, no. 7, Apr. 2023, Art. no. 2201638.
[50] W. Li et al., "Self-powered and high sensitivity ionic skins by using versatile organogel," *Nano Energy*, vol. 99, Aug. 2022, Art. no. 107359.
[51] Y. Wu, L. Cai, G. Chen, F. Yang, and M. He, "3D printed, environment tolerant all-solid-state capacitive ionic skin," *J. Mater. Chem. A*, vol. 10, no. 35, pp. 18218–18225, 2022.
[52] Y. Shi et al., "Flexible capacitive pressure sensor based on microstructured composite dielectric layer for broad linear range pressure sensing applications," *Micromachines*, vol. 13, no. 2, p. 223, Jan. 2022.
[53] X. Fu et al., "A high-resolution, ultrabroad-range and sensitive capacitive tactile sensor based on a CNT/PDMS composite for robotic hands," *Nanoscale*, vol. 13, no. 44, pp. 18780–18788, 2021.